

Coverage-Mapping Method Based on a Hardware Model for Mobile-Robot Positioning in Intelligent Spaces

Ernesto Martín-Gorostiza, Fco Javier Meca, José Luis Lázaro Galilea, Eduardo Martos-Naya, Fernando B. Naranjo, and Óscar Esteban

Abstract—In this paper, we describe a method for relating the precision in phase shift measurements to the navigation areas in which that precision is reached so that a coverage map is built, setting a signal-to-noise ratio (SNR) threshold level that depends on that phase precision. The method brings a novel approach to linking different areas in robotics and is applied to a mobile-robot (MR) local positioning system (LPS) in an intelligent space, where distances are computed from differential phase shift measurements with intensity modulation and direct detection (IMDD) infrared signals. A global model including the parameters of all the parts involved, e.g., optoelectronics, wireless channel, and instrumentation hardware, is developed. Furthermore, based on the model, an analytical expression deduced for the phase shift measurement is used to find the necessary SNR for a desired precision. A complete set of results, applying the coverage cells to a real building covering a path followed by an MR, is shown. The position of the MR can be known, with an accuracy value below 5 cm and tested in a basic rectangular locating cell with dimensions $3.0 \text{ m} \times 2.5 \text{ m}$.

Index Terms—Coverage mapping, infrared (IR), intelligent spaces, local positioning system (LPS), mobile robotics, positioning.

I. INTRODUCTION

A. Framework. Positioning in Intelligent Spaces

An intelligent space (IS) is an environment capable of controlling the processes, managing the tasks, and taking decisions concerning the elements, including humans, that integrate the said space. It must be provided with a powerful (multi-)sensorial system, reference points (RP), landmarks, emitters, and different types of receiver, which can, in turn, also act

as beacons, and so on; it must also include the channel infrastructure for signal transport and one or more nodes where computing tasks take place. The importance of this kind of system has increased in recent years in applications where the building itself is responsible for both industrial and civil applications. Some authors have concentrated their effort in recent years to formalizing the definitions concerning these spaces and created the basis for the structure and architecture of such intelligent environments [1], [2]. In the specific area of mobile-robot (MR) navigation in an IS, the intelligence of the system lies within the environment, rather than in the MR, which remains relatively simple. This design philosophy is also present in [3], where advanced ideas along this line are developed; a distributed intelligent network where robots and sensors collaborate for indoor 3-D localization and navigation purposes is shown in this paper. Similar aims were achieved for outdoor robot navigation in [4]. Of the numerous tasks that the system intelligence must deal with, knowing the position of the MR is essential. In [5], rigorous definitions are given for formalizing the topological aspects related to a localization space. In intelligent indoor environments, a local positioning system (LPS) can be implemented in different ways. Wireless location, making use of wireless local area networks already installed in the buildings, has led to indoor radiolocation [6]. For outdoor environments, global positioning system (GPS) is still the only means of positioning with radio signals. For indoor environments, however, cameras are the most widely used devices and can, for instance, receive the image of a landmark placed on the MR or an infrared (IR) signal emitted by it [7]. Geometrical parameters, such as distances or angles, are then extracted from the image captured by the camera [8], and the position of the MR is obtained by image-processing algorithms, achieving average precisions of about 5–10 cm. A brief explanation distinguishing RF, IR, and ultrasound-based positioning systems is also given in [7], and although ultrasounds are seldom used for positioning, they are used for other applications in robotics, such as obstacle detection or environment modeling. Finally, whichever technology is chosen for locating an MR, there is a need to measure, or calculate, geometrical parameters, i.e., angles or distances. Location with IR in a space conceived as stated, but using optoelectronic devices instead of cameras, is not, in practice, widely used. However, under certain working restrictions, an LPS developed like a GPS for indoor applications, making use of IR instead

Manuscript received July 28, 2008; revised January 26, 2009. First published August 18, 2009; current version published January 7, 2010. This work was supported in part by the Spanish Research Program through Project SILPARII DPI 2006-05835 and in part by the University of Alcalá Research Program “Diseño y optimización de un sistema de localización basado en infrarrojos para sistemas de posicionamiento local” under Contract UAH PI2005/075. The Associate Editor coordinating the review process for this paper was Dr. John Sheppard.

E. Martín-Gorostiza, F. J. Meca, J. L. Lázaro Galilea, F. B. Naranjo, and Ó. Esteban are with the Department of Electronics, University of Alcalá, 28871 Madrid, Spain (e-mail: ernesto@depeca.uah.es).

E. Martos-Naya is with the Department of Communications Engineering, University of Malaga, 29071 Malaga, Spain.

Color versions of one or more of the figures in this paper are available online at <http://ieeexplore.ieee.org>.

Digital Object Identifier 10.1109/TIM.2009.2023146

of RF signals, would be very convenient. This may be the case when opacity between two neighbor rooms is needed or when other RF devices could interfere. A comparative analysis between the use of RF or IR can be seen in [9]. The existing devices for IR distance measurement are the range finders, or telemeters, which for middle-range distances, of up to about 50 m, have been classically working by phase shift measurements [10], and the latest approaches offer measurement precisions below 1 cm [11]. During the last few years, new techniques for IR range finders based on very accurate time-of-flight measurements have been developed by Kilpela [11] and Kostamovaara *et al.* [12]–[15]. A telemeter works very satisfactorily when measuring distances from point to point in a straight line, having a front-end optical arrangement to collect a lot of energy and send it to the photodetector placed in the focal plane. The signal-to-noise ratio (SNR) at the photodetector is then large enough to reach those precisions, but the system's field of view (FOV) is not wide enough to be suitable for MR positioning. On the contrary, improving the FOV yields less energy collection and worsening SNR, which implies less measurement accuracy, so that achieving an accuracy of 1 cm with an acceptable FOV becomes very difficult indeed. However, for an IR-LPS, a system with a wider angle is needed so a telemeter cannot be used in its original form, unless it is mounted on a spinning mechanical device, or a specific system for emitting at different angles, as in [16], although in this case, high accuracy is difficult to achieve; in robotics, for active laser-ranging issues, scanning laser-range finders are used [17]. IRs are currently used for wireless communication in environments with the kind of infrastructure needed for an IS; the studies and approaches developed by Kahn *et al.* in this area since the mid-90s are remarkable [9], [18]. Finally, the position of the MR that is navigating inside the IS must be obtained by solving a classical set of triangulation equations [19]–[21], by using the so-called spherical trilateration, as was the case with the GPS at first, or it leads to hyperbolic trilateration, when the differences of the magnitudes (phase shift, time of flight, etc.) are measured instead [22]. However, there is still one essential issue remaining: knowing the areas where the position is obtained with a certain required precision. This matter of coverage areas is a crucial issue in mobile telephony, where coverage is a question of enough signal level. In MR navigation applications, it is treated specifically in each case and is often solved by geometrical methods, as in [23] for an indoor RF application. Finally, it must be stressed that in an IR-LPS, there is a severe tradeoff between FOV and SNR at the detectors, and between the directionality of the emitter and SNR at the detectors as well, which implies a severe tradeoff between precision (depending on the SNR) and coverage. The advantages compared to counterpart systems based on cameras or radio are mainly the cost, much less computational charge compared to the former, and the lack of interference between different rooms with respect to the latter. Most of the work done in this area treats low-level instrumentation and high-level localization and navigation aspects separately. In [24], an in-depth analysis of the sensors of the system allows us to link hardware considerations to localization and map building for greater accuracy.

The aim of this work, which brings a novel approach to the field of robotics, is to propose a method for connecting the precision in the phase shift measured by the hardware (i.e., the precision in the final MR position) to purely navigational and positioning aspects, in this case the building of a coverage map, where the MR is to be positioned with a known precision. A precision in the phase shift corresponding to 1 cm at the operating frequency is sought. This method is applied in an LPS previously proposed by the authors and is referred to in [25], which is developed within the philosophy design context already mentioned [1], [2]. Although the objective is to propose the aforementioned method, some remarks about the instrumentation system have also been included for better comprehension.

For this purpose, a model including all the segments, stages, and elements of the whole system has been developed, taking into account the parameters of emitter, detector, the aerial wireless channel, and the instrumentation hardware, as well as an accurate study of the noise in the system. Based on this model, a mathematical expression of the measured phase shift has been deduced, which allows precision in the phase shift to be connected to a SNR threshold level SNR at any of the locating RPs, which are, in turn, the receivers. This connection is the key concept of the method, as will be explained. The SNR threshold value defines whether an area is under valid coverage or not. Using this criterion, the coverage map in the MR movement space can be traced. The movement velocity of the MR have also been taken into account. As in the case of [21], this method will be an extremely important tool as a software aid to LPS design and the evaluation of possible improvements in the system before carrying them out.

A comment about terminology in this paper must be made before going any further. The phase shift differences that this work refers to correspond to the differences in the time of arrival; in this paper, the term differential phase shift of arrival (DPOA) will be used for similarity and simplicity.

II. GENERAL DESCRIPTION OF THE WHOLE SYSTEM

A. IR-LPS

In this paper, the LPS is based on IR differential phase shift measurements, working with intensity modulation and direct detection (IMDD). The LPS operates with only one wavelength so that no ambiguities in the number of wavelengths exist. The conceived LPS is depicted in Fig. 1, where the transmitter, an IR led (IRED) on board the MR, is the point whose position is to be measured. A basic locating cell (BLC) composed of five receivers, namely, RP_1, \dots, RP_5 , which are placed in the MR environment, is shown. Each receiver is a sensor that includes the detecting device and an electronic circuit for optical-to-electrical signal conversion. The hardware module (hw) also deployed in a lower level block diagram in the same picture is placed at the central intelligent node (CIN) and will be explained in the next part of this section. Both the sensors and the hw block have been specifically designed for this application. Thus, the whole hw design consists of the signal reception stage placed at each one of the receivers and a two-stage in-phase and quadrature (I–Q) demodulator based on a classical vectorial lock-in structure, which is implemented for

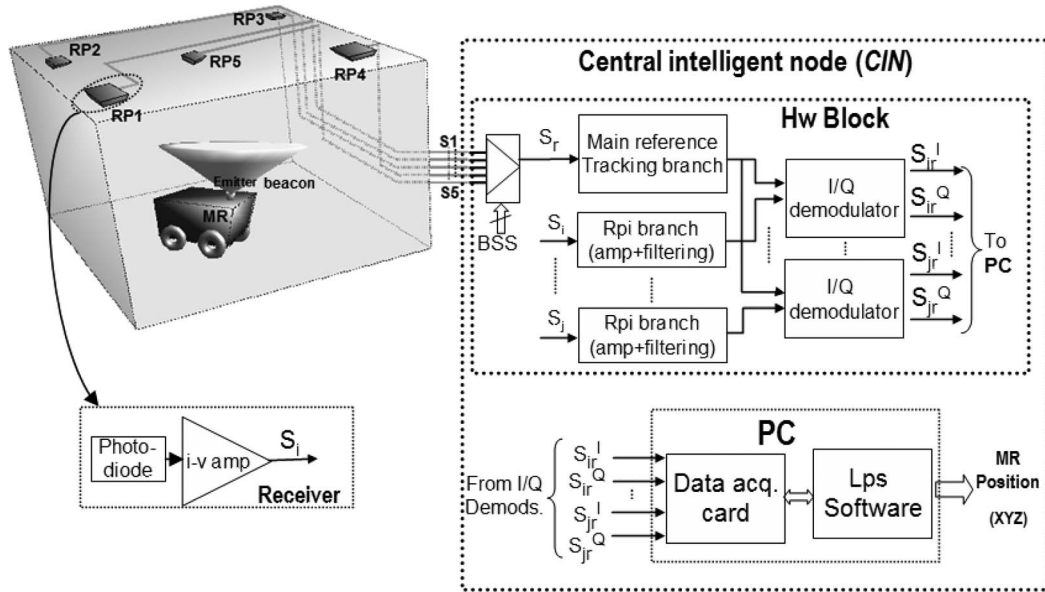


Fig. 1. Conception of the IR-LPS. S_r corresponds to the signal of the main reference point chosen. The DPOAs are obtained between the rest of RPs in the cell and this main reference.

every pair of receivers, as detailed in the following point. In this LPS scenario, the MR to be located carries on board the emitting beacon (i.e., the IR transmitter), and every receiver acts as a locating RP. Signals delivered by the RPs are multiplexed so that any of them can be dynamically chosen as the main RP; this operation is carried out by the digital selection signals best-signal selection shown in the figure. The position is obtained on the computer, in the CIN, from the differential phases between the signals at every RP in the BLC and the main RP.

For 3-D location, if the height of the MR is known and constant, a minimum of four RPs would be needed when working with single differences of distances to those RPs [22]. It is common practice to provide the system with a higher number of RPs so that better accuracy is achieved when solving the set of equations with noisy measurements [26]. In this paper, five RPs have been chosen as a good tradeoff solution in order not to use too many receivers. In regard to the BLC shape, the idea of having cells with different geometry suitable for the particularities of the area to be covered was treated in [27]. Some coverage considerations were made in that work as well, but based only on geometrical aspects. The optimal location of the RPs in this kind of indoor system, treated by some authors as in [28] for cameras, is a wide open research area. In this paper, a symmetrical distribution of the RPs, one in each corner and one in the center, is proposed. By default, the central RP is chosen as the main one, but the system can use any of the others, as explained in the previous paragraph.

A very important question to be taken into account in this paper is that the precision that is sought for the measured magnitude is the phase. The precision in phase is directly related to the corresponding one in distance by a constant factor $\Delta\phi \cdot (C/360f)$, which is a typical telemeter equation [29], with $\Delta\phi$ being the phase shift precision in degrees and f being the frequency. This accuracy is, in turn, demanded by the system in charge of solving the positioning equations for the MR once a precision in the MR position is desired.

B. Hardware: The Differential Phase Measurement Module

A measuring structure has already been proposed in [30]. Here, an improved module developed from that one is shown in Fig. 2, where the different parts have been related to the blocks depicted in Fig. 1. Only the circuit branches corresponding to the main RP, i.e., RP_r , and a generic RP_i are depicted, maintaining the same structure for the rest of RP_j as for RP_i . In Fig. 2, the multiplexer has been removed as it is only an auxiliary component. The emitted signal is an IMDD-IR signal modulated at a carrier frequency f_0 , in our case 4 MHz. This optical signal $S_{i(op)}$, with its carrier flight phase shift Φ_i , is collected at each receiver RP_i . Every RP_i has a first detection stage with an identical design for all of them, which is implemented in the sensor. This stage includes the detection device and a basic transimpedance amplifier for optical-to-electrical conversion so that a voltage signal V_i is obtained. All the rest of the hw is implemented at the CIN. The second stage is designed for signal conditioning, built with a high bandwidth operational amplifier followed by a wideband bandpass filter. The main reference branch includes a tracking stage, an RT stage in the figure, which comprises a phase-locked loop (PLL) for clean signal recovery and a local oscillator LO that generates two low-frequency I-Q signals V_L and V_Q , with ± 1 amplitude levels and a 32-kHz frequency. In Fig. 2, the phase shift Φ_{ir} is the relative DPOA between the signals at RP_i and RP_r , i.e., $\Phi_{ir} = \Phi_i - \Phi_r$. The third stage is a low-frequency conversion stage, where the signal V_i is shifted down to f_L (8 kHz), using the signal V_{rL} shown in the figure, keeping the relative DPOA Φ_{ir} unaltered. The signal V_{rL} is generated in the *upper single-side-band* (USSB) block, removing the lower band in its frequency spectrum. Therefore, only the right-side contributions, given by the odd harmonics of f_L , aside from each odd harmonic of f_0 , are present. This is extremely important, as otherwise, the phase information, which is contained in one of the two final dc signals would be removed by cross cancellation between the upper and lower

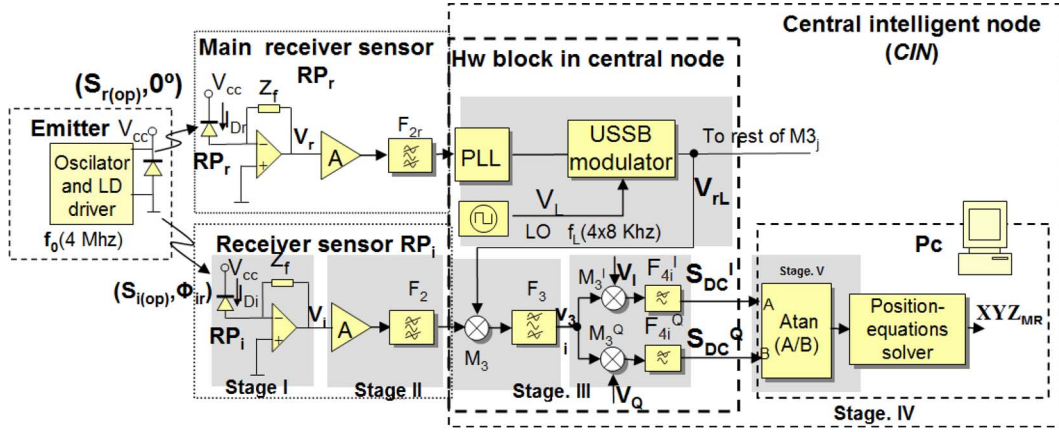


Fig. 2. Hardware diagram.

bands. The USSB block is a standard structure for this purpose [31]. In this block, V_L is frequency divided by four, and V_I and V_Q are generated at the 8-kHz frequency f_L . These two signals are necessary for lower band suppression in the USSB module and are to be used further in the I-Q demodulating block as well. Finally, the two dc signals S_{dc}^I and S_{dc}^Q are obtained from this I-Q demodulation structure, at the output of the fourth stage. From these dc signals, the original DPOA corresponding to the phase shift between $S_{r(op)}$ and $S_{i(op)}$, i.e., Φ_{ir} , is computed at the fifth stage and implemented on the PC, where an arctan function is carried out. Finally, the set of measurements Φ_{ir} is used to calculate the position of the MR, i.e., $(XYZ)_{MR}$, using trilateration techniques, as mentioned earlier.

III. RADIOMETRIC MODEL OF THE FIRST SEGMENT

The first segment of the whole model includes the emitter device, the aerial wireless link, the detecting device, and the elemental electronic circuit for optical-to-electrical signal conversion, consisting of a current-to-voltage converter, hereafter referred to as the $i-v$ converter. The emitting block is composed of a stable and precise voltage-controlled crystal oscillator (VCXO) oscillator with a ± 100 ppm frequency-precision circuit driving an IRED. This precision is enough with respect to its influence on the final precision of the measured phase shift as other error sources have a greater affect, as has been proven experimentally. Stability in the emitter is necessary as in this application it is important to design a very narrow band output filter for the PLL so that phase noise is reduced as much as possible in the reference-tracked signal, and any drifts or frequency jitters in the frequency of the original signal would make this difficult.

Fig. 3 shows the geometry of emission and detection; the optical emission pattern is described in terms of the optical power delivered per solid-angle unit, maintaining rotational symmetry with respect to the azimuth angle φ , therefore, the emitted power is a function of the observation angle θ_e , as shown in the figure. In this paper, the real pattern of the commercial emitter used is introduced in the model by experimental characterization of the power emitting shape and further curve

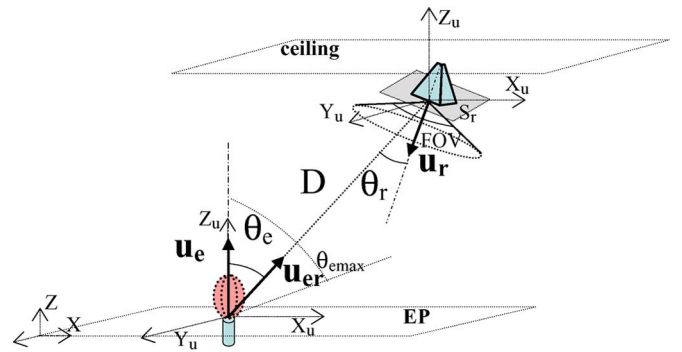


Fig. 3. Emission-detection geometry. Emission origin is in the emitting plane (EP). Detector is placed in the ceiling

fitting so that a n th-order generalized Lambertian pattern is accurately fitted to the real one. With similar considerations as in [9], the electrical current rms value at the i th detector, i.e., I_{0i} , provided by the photodetector, is

$$\begin{aligned}
 I_{0i} &= E_e \cdot A_s^* \\
 &= \rho(\lambda) \cdot \left(\frac{P_{emx} A_s^*}{D_i^2} (u_e \cdot u_{eri})^n (-u_{eri} \cdot u_{ri}) \Pi \left(\frac{\theta_{ri}}{FOV^*/2} \right) \right)^2 \\
 &= \rho(\lambda) \cdot \left(\frac{P_{emx} A_s^*}{D_i^2} \cos^n(\theta_{ei}) \cos(\theta_{ri}) \Pi \left(\frac{\theta_{ri}}{(FOV^*/2)} \right) \right)^2
 \end{aligned} \tag{1}$$

where

$$\Pi \left(\frac{\theta}{W} \right) = \begin{cases} 1, & \text{if } \theta < W \\ 0, & \text{if } \theta > W \end{cases}$$

where index i stands for the i th receiver, but only for those variables that depend on the receiver under consideration, while the rest of the variables keep the same values for all of them. P_{emx} is the peak emitting power, A_s^* and FOV^* are the effective sensitive area and the effective FOV of the photodetector, which will be explained at the end of this paragraph, and $\rho(\lambda)$ is a matching factor that includes detector responsivity and emitter efficiency, both of which depend on the optical wavelength.

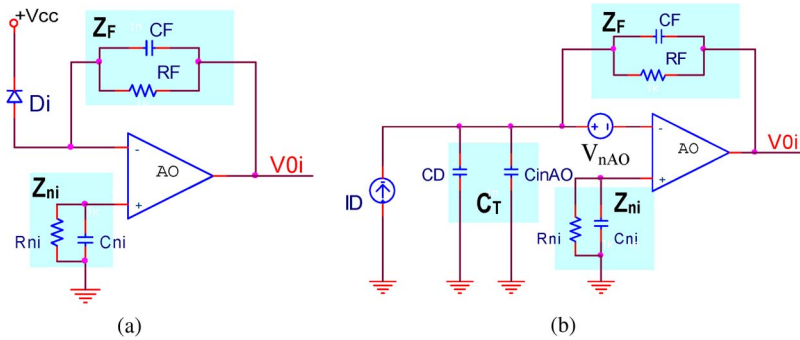


Fig. 4. Transimpedance amplifier to obtain a voltage signal at the i th receiver. Circuit used. (a) Right model. (b) Equivalent model.

D_i is the distance between the emitter and the i th detector, and n is the index of the generalized Lambertian optical emission pattern fitted to the emitter. The angle θ_e is the observation angle, i.e., the angle at which the radiated power is to be considered. As can be seen in Fig. 3, θ_e is measured from the maximum emitting direction that holds for $\theta_e = 0^\circ$, whereas θ_{ri} is the reception angle at the i th detector, measured from the detector's central axis, orthogonal to its surface. For design purposes, the cosines of the angles are expressed in terms of scalar products between the unitary orientation vector at the emitter pointing toward the maximum emission direction \mathbf{u}_e , the unitary orientation vector at the receiver pointing in the direction of the central axis \mathbf{u}_r , and the unitary vector in the emitter–detector direction \mathbf{u}_{er} . The expression in the third term of (1) is the form in which it is actually managed in the programmed model. The expression in the fourth term of (1) is written for a more user-friendly geometrical visualization. The square-window function $\Pi(\theta)$ of the reception angle takes into account the fact that there is no energy received beyond FOV^* (this term in the expression is correct considering that the FOV^* is bigger than the emitting angle, which is the case in our system). A line-of-sight (LOS) IR link has been considered for the model. Some authors have proposed models for the IR wireless channel in indoor environments, taking into account secondary multipath contributions. Some attempts at modeling it as an environment-dependent low-pass filter have been made [32], [33] as well. In [34], the same study is focused on indoor RF systems for geolocation with TOAs. As can be seen in [35], corners are the critical areas when working with one single emitter, but at a distance of about 60 cm from the corners, the effects of second contributions are unappreciable for a room with a common surface. In our setup, in the corners, a distance of 70 cm to the walls is kept uncovered by the BLC, and measurements ascertain the nonappreciable influence of secondary contributions. Hence, the channel transfer function only affects the signal by a TOA delay, and an attenuation coefficient with value $\cos^n(\theta_{ei})D_i^{-2}$.

As we have said, A_S^* is not the sensitive area of the photodetector itself, but is the effective area, including the effects of the optical arrangement fitted to improve the SNR. The effects of the optical elements have been modeled as well so that they can be included and managed in the whole model. In this case, A_S^* is an improved detection area, obtained by an optical set in which the original detector with area A_S , is placed out of focus, at a distance of s' from a convergent

lens of focal distance f' . The FOV is also affected by this arrangement so that FOV^* is considered instead. Taking into account considerations of geometrical optics [36], the following expressions can be deduced for both effective parameters:

$$A_S^* = \frac{1}{\beta^2} A_S \quad \text{FOV}^* = \arctan \frac{L \cdot f' + R_l(f' - s')}{(f')^2 - (f' - s') \cdot f'}$$

with

$$\beta = \frac{s'}{s}; \quad s = \frac{f' s'}{f' - s'} \quad (2)$$

where L is the size of the square-shaped detector, and R_l is the lens radius. The factor $\beta < 1$, is obtained from the equivalent distance s in the object space between the equivalent detection plane and the lens plane.

The circuit for optical-to-electrical conversion, as shown in Fig. 4(a), is the $i-v$ converter already mentioned. It is a classical transimpedance stage where the components have, nevertheless, been carefully chosen to meet propagation time stability constraints. In Fig. 4(b), the equivalent model of the circuit is displayed. At its output, frequency-dependent signal and noise contributions are present.

The feedback impedance z_F for $i-v$ conversion is formed by a resistor R_F and a shunt capacitance C_F , fitted for response time stability purposes, as has been mentioned. The impedance Z_{ni} is added at the noninverting terminal for radiated noise cancellation. C_D is the photodiode junction capacitance, C_{inAO} is the operational input capacitance, and e_{nAO} is its equivalent input noise voltage. A classical analysis of this circuit provides the expressions for the transfer function of the stage as well as the noise transfer function and the noise referred to the output, i.e., referred to output (RTO) noise, which will be outlined in the following paragraphs. Considering the following expressions for the circuit:

$$A_o(j\omega) = \frac{A_{vo}}{1 + j\omega/w_{cH}} \quad A_F(j\omega) = \frac{R_F}{1 + A_o(j\omega)}$$

$$C_e = C_T + C_F [1 + A_o(j\omega)] \quad C_T = C_{inAO} + C_D \quad (3)$$

where $A_o(j\omega)$ is the open-loop operational amplifier voltage gain, and C_T is the total input shunt capacitance, i.e., the sum

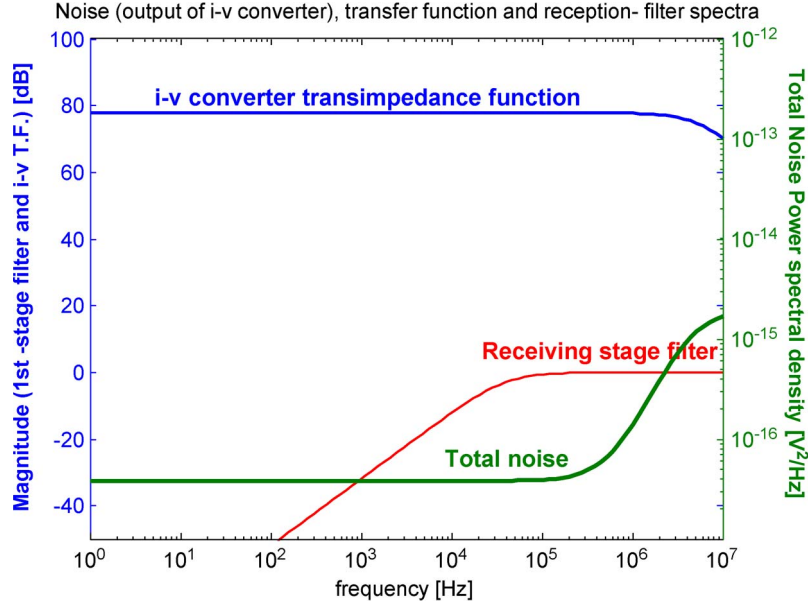


Fig. 5. Transfer function spectrum and RTO noise spectrum for the $i-v$ converter. The 3-dB cutoff frequency of $Z(j\omega)$ corresponds to maximum time-delay stability.

of C_{inAO} and C_D . The ideal noncorrupted output voltage signal delivered by the $i-v$ converter would be

$$v_i(j\omega) = i_D \cdot Z(j\omega) = i_D \cdot A_o(j\omega) \frac{A_F(j\omega)}{1 + j\omega A_F(j\omega) C_e(j\omega)}. \quad (4)$$

In (4), $Z(j\omega)$ is the frequency-dependent transimpedance transfer function of the circuit in Fig. 4, I_D is the sinusoidal current whose rms value is given by (1) at frequency f_0 . On the other hand, the total output voltage signal v_i is corrupted by additive noise, i.e.,

$$v_i^*(j\omega) = v_i(j\omega) + n_i(j\omega) \quad (5)$$

with v_i being the noncorrupted signal given by (4) and n_i the additive Gaussian RTO noise in the $i-v$ converter, with a non-flat-frequency distribution due to the effect of the frequency-dependent noise transfer function of the stage. All noisy contributions n_{op} are statistically uncorrelated, and hence, the noise power spectral density at the output of the first stage $N_{0i,f}$, writing $2\pi f$ instead of ω , is

$$N_{0i,f} = \sum_p n_{ip}^2 = (V_{nAO})^2 \frac{1 + (2\pi f R_F (C_F + C_T))^2}{1 + (2\pi f C_F R_F)^2} + \left(\frac{4K_B T}{R_F} + I_{DN}^2 + i_{nAO}^2 \right) \frac{R_F^2}{1 + (2\pi f C_F R_F)^2} \quad (6)$$

which is expressed in square volts per hertz. The frequency dependence of the noise power is explicitly noted by the subindex f . K_B is the Boltzmann constant, T is the absolute temperature, I_{DN} is the noisy current associated with the detector photocurrent, and i_{nAO} is the AO input noise current. In Fig. 5, the magnitudes of the transfer function $Z(j\omega)$ and the first stage filter as well as the RTO noise spectra are depicted. As the signal is a pure sine signal, the effect

on the input signal is a multiplicative constant given by the magnitude of $Z(j\omega)$ and a very stable time delay produced by the phase shift of this stage, which is automatically removed when taking the difference of phases between each pair of receivers. The fact of being stable is of extreme importance because any random change in time would not be removable. Hence, C_F and R_F have been chosen so that the time delay introduced by the $i-v$ stage maintains the maximum stability, either against any temperature drifts or supply voltage variations.

IV. EFFECTIVE SNR

If the SNR were computed at the output of the $i-v$ converter, the value obtained would seem to be quite disadvantageous to any expectations of a good result, as it could well be below 0 dB. In fact, however, after the whole processing stage, sine signals are narrowly filtered, and the final incident noise power is lowered enormously. Let us define an effective SNR, denoted as SNR_{eff} , that is computed as the ratio between the power of the signal at the output of the third stage (*stage III* in Fig. 2) and the final total additive noise power at the output of the fourth stage. This magnitude is the key link in this work to connecting the definition of the positioning areas for the MR in the coverage map with the estimated precision of the differential phase, as will be explained in Sections V and VI. This SNR_{eff} is defined at this point because it is the last before the sine carriers are removed in the final I-Q demodulating block. The SNR defined this way is very suitable for analytical purposes as its connection with the final phase-measuring estimator is easily laid out, as shown in Section V. The analytical background for deducing the expressions of the signals that appear in this paper can be seen in [37] for a classical I-Q demodulation structure in a lock-in amplifier. Considering the signal V_{RT} in Fig. 2, and proceeding as in [37], it can be deduced that the signal at the

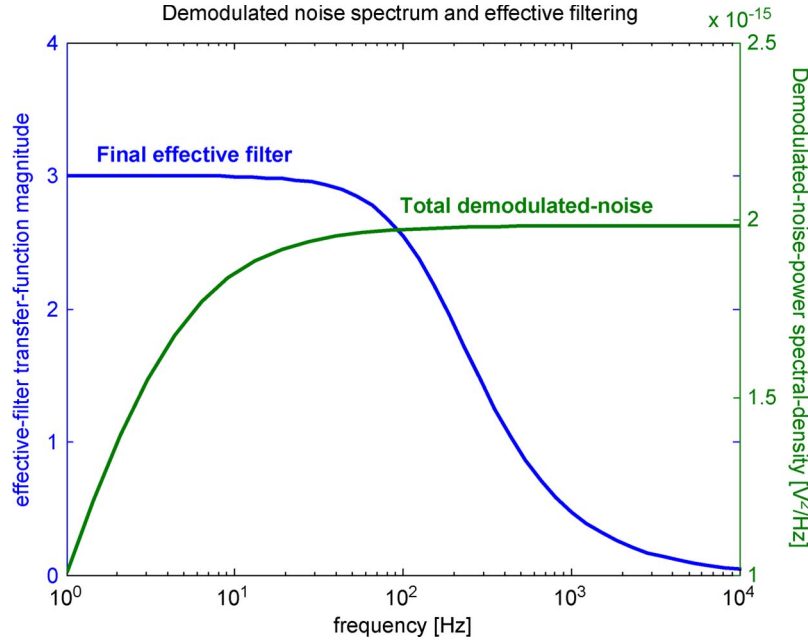


Fig. 6. Final effective-noise spectral power density and effective-noise bandwidth after demodulation. Note that the scale for noise is the right-hand-side axis starting at a value of $1 \cdot 10^{-15} \text{ V}^2/\text{Hz}$.

output of the low-frequency conversion stage can be expressed in the time domain

$$v_{3i}^* = v_{3i} + n_{3i} \quad (7)$$

$$v_{3i} = K_{3i} \left\{ \sum_{n=0}^{\infty} \frac{1}{2n+1} [\cos(2\pi(2n+1)f_L t + (\phi_{ir} + \phi_{3i} + n_{\Phi}) + (2n+1)\phi_L)] \right\} \quad (8)$$

where v_{3i} is the signal of interest, and n_{3i} is the additive noise, which will be explained further. K_{3i} is the global multiplying constant after all previous filters or multipliers; it also includes the amplitude of the original signal received by the detecting receiver, the amplitude of the output signal of the PLL, i.e., V_{rPLL} , and the constants contained in the Fourier series correspond to v_I and v_Q . The f_L parameter is the intermediate low frequency to which the signal has been demodulated. The term Φ_{3i} is a deterministic error in phase, removable by calibration, which comprises all the accumulative phase shifts up to the third stage introduced by the elements of each previous one, while n_{Φ} is a random nonremovable phase noise introduced by the PLL, which is modeled using a linear model of the PLL proposed by Proakis and Salehi [38]; ϕ_L is the phase difference between the signals V_I and V_{rT} shown in Fig. 2. The noisy contribution n_{3i} is the Gaussian additive noise coming from the i - v stage, given by (6), with a non-flat-frequency distribution after the filtering and demodulation process followed up to this point. The final effective-noise equivalent bandwidth of the whole system BW_N is determined by the bandwidth of the last filter F_4 , as after the whole demodulation process the noise spectrum has been shifted down to low frequencies, with a shift decrement $f_0 + (2n+1)f_L$ (for $n = 0, 1, 2, \dots$). Thus, the final effective-noise spectrum is obtained from the original spectrum $N_{0,f}$, moved to the zero-frequency point,

and the aliases of $N_{0,f}$ shifted to frequency values $(2n+1)f_L$ weighted by factors $1/(2n+1)$, each one due to the harmonics contained in V_{rL} , all filtered by F_{4i} . In Fig. 6 the final effective-noise equivalent bandwidth of the whole system BW_N and the noise contribution corresponding to $n = 0$ are shown. The $\text{SNR}_{\text{eff}}^I$ is then obtained as

$$\begin{aligned} \text{SNR}_{\text{eff}}^I &= 10 \log \left(\frac{s_{3i}}{N_i^I} \right) = 10 \log \left(\frac{\frac{1}{2} (K_{3i})^2 \sum_{n=0}^{\infty} \frac{1}{(2n+1)^2}}{N_i^I} \right) \\ &= 10 \log \left(\frac{\pi^2/16}{N_i^I / (K_{3i})^2} \right). \end{aligned} \quad (9)$$

For total noise spectral density power integration, it is perfectly reasonable to consider a first-order filter with a 3-dB cutoff frequency at 32 Hz as flat in the frequency range covered by F_4 . A comment about the choice of this bandwidth is made at the end of Section V-A. The total noise power is thus obtained

$$\begin{aligned} N_i^I &= (K_{N3i})^2 (K_{04i}^I)^2 \sum_{n=1}^N N_n \\ &= (K_{N3i})^2 (K_{04i}^I)^2 \sum_{n=1}^N \int_{-\infty}^{+\infty} N_{n,f}(f) |H(f)|^2 df \\ &= (K_{N3i})^2 (K_{04i}^I)^2 BW_N \sum_{n=1}^N \frac{\eta_n}{(2n+1)^2} \end{aligned} \quad (10)$$

with

$$\eta_n = N_{0,f}|_{f=f_0+2nf_L}.$$

The constant $K_{N_{3i}}$ is the accumulative noise multiplicative constant throughout the first three stages, and K_{04i}^I is the multiplicative constant of only the fourth stage. In (9), the signal power has been computed as the average power of the sinusoidal components of v_{3i} in (7), and N_n represents the aliased noise power terms corresponding to the noise components mentioned in previous paragraphs due to the harmonics of the signal V_i in Fig. 2. Identical expressions can be written for the Q branch, but with the superindex Q instead. It is convenient to define the *normalized noise* with respect to $K_{4i}^I = K_{3i}K_{04i}^I$ for the I branch (the same definition stands for the Q branch using K_{4i}^Q) so that the SNR handled in (9) can be related to a unity amplitude signal v_{3i} . This definition is also useful for subsequent analysis, as will be seen. In doing so, SNR_{ieff} in (9) can be written using a compact notation for both I and Q branches together as

$$\begin{aligned} \text{SNR}_{\text{ieff}}^{I,Q} &= 10 \log \left(\frac{(\pi^2/8) \left(1 / \left(K_{04i}^{I,Q} \right)^2 \right)}{N_i^{I,Q} / \left(K_{3i} \right)^2 \left(K_{04i}^{I,Q} \right)^2} \right) \\ &= 10 \log \left(\frac{(\pi^2/16) \left(1 / \left(K_{04i}^{I,Q} \right)^2 \right)}{\overline{N}_i^{I,Q}} \right) \end{aligned} \quad (11)$$

where

$$\overline{N}_i^{I,Q} = \frac{N_i^{I,Q}}{\left(K_{3i} \right)^2 \left(K_{04i}^{I,Q} \right)^2} \quad (12)$$

is the normalized noise power spectral density, with the normalizing factor K_3 as explained earlier and with N_i obtained as stated in (10). In these expressions, only one of the indexes, i.e., I or Q, must be considered for I or Q branches, respectively. On the other hand, in the time domain, the instantaneous normalized final noise is, in the form that will appear in the estimator explained in the following sections, given by

$$\overline{n}_i^{I,Q} = n_i^{I,Q} / K_4. \quad (13)$$

V. DIFFERENTIAL PHASE ESTIMATION ANALYSIS

At this point, it is necessary to make some comments concerning the fifth stage (Fig. 2). An expression for the DPOA has been deduced with this model for a generic pair of RPs (receivers), where one of them is the common reference and the other is a generic i th reference. Therefore, an expression $\hat{\Phi}_{\text{ir}}$ for the final measurement of the DPOA sought is deduced, and it is written as

$$\hat{\Phi}_{\text{ir}} = \arctan \left(\frac{K_{04}^I \cdot \sin(\phi_{\text{ir}} + n_\phi + \phi_4^I) + \frac{n^I}{K_{3i}K_{04i}^I \frac{\pi}{4}}}{K_{04}^Q \cdot \cos(\phi_{\text{ir}} + n_\phi + \phi_4^I) + \frac{n^Q}{K_{3i}K_{04i}^Q \frac{\pi}{4}}} \right)$$

$$= \arctan \left((1 + \Delta K) \frac{\sin(\phi_{\text{ir}} + n_\phi + \phi_4^I) + \frac{\overline{n}^I}{\frac{\pi}{4}}}{\cos(\phi_{\text{ir}} + n_\phi + \phi_4^I) + \frac{\overline{n}^Q}{\frac{\pi}{4}}} \right) \quad (14)$$

with

$$\phi_{\text{ir}} : \text{true value} \quad \Delta K = \frac{K_{04}^I - K_{04}^Q}{K_{04}^Q} \quad \overline{n}^{I,Q} = \frac{n^{I,Q}}{K_{3i}K_{04i}^{I,Q}}. \quad (15)$$

The term ΔK is a gain error due to the unavoidable interbranch deviation existing between the I and Q paths in the fourth stage, although identical components are chosen for both on a monolithic substrate. K_{04i}^I and K_{04i}^Q are the multiplying constants at the I and Q branches, respectively; the former takes account of the constants of the multiplier M_4^I and the filter F_4^I , and the latter of M_4^Q and F_4^Q , as shown in Fig. 2. In (14), $\hat{\Phi}_{\text{ir}}$ is the estimation of the measured value of the phase shift. The true value of the DPOA searched is ϕ_{ri} . Ideally, if no noise was present and no hardware real effects were considered, ΔK , \overline{n}^I , \overline{n}^Q , ϕ_4^I , ϕ_4^Q , and n_ϕ would be zero. The phase shift terms ϕ_4^I , ϕ_4^Q are the accumulative phase shift errors and may be considered as a constant phase offset. The phase noise term n_ϕ comes from the PLL in the reference branch. Its typical deviation has been modeled as a function of the SNR in the PLL, as shown in Section V-A. Normalized noises \overline{n}^I and \overline{n}^Q are the ones defined in (13) and expressed in (14) in the time domain, with the distinction made for the two branches I and Q, distinguished in two terms with indexes I and Q because although they have different instant values, they have the same Gaussian statistical distribution, as they have the same total average noise power integrated in the frequency domain. To quantify the error in the measurement of the DPOA, the expression in (14) is pseudoanalytically analyzed by simulation, as explained in the next point.

A. Effective SNR and Precision

There is an intrinsic relation between the quality of the signal level against noise, i.e., SNR, and the precision of the estimated DPOA, which can be studied by analytical simulation of (14), as mentioned earlier. Therefore, for a certain desired precision in the estimation of the DPOA, a minimum value of SNR at every receiver must be reached. The restriction for SNR is not found directly at the reception stage, but is set for the effective SNR, i.e., SNR_{eff} , which has already been defined, instead. This is much more suitable because of the direct relation between SNR_{eff} and the noise terms that appear in the final Φ estimator, as can be seen in (11), (12), and (14). For simulation-aided analysis of the estimator and finding the empirical restrictions of SNR_{eff} as a function of precision, the programmed algorithm obeys the procedure shown in the flowchart in Fig. 7. The gain error ΔK , the SNR in the PLL (SNR_{PLL}), and the effective SNR (SNR_{eff}) are considered as simulation parameters, each one swept in a range of values. The analysis is performed for a range of phase values from 0° to 80° . The error is computed

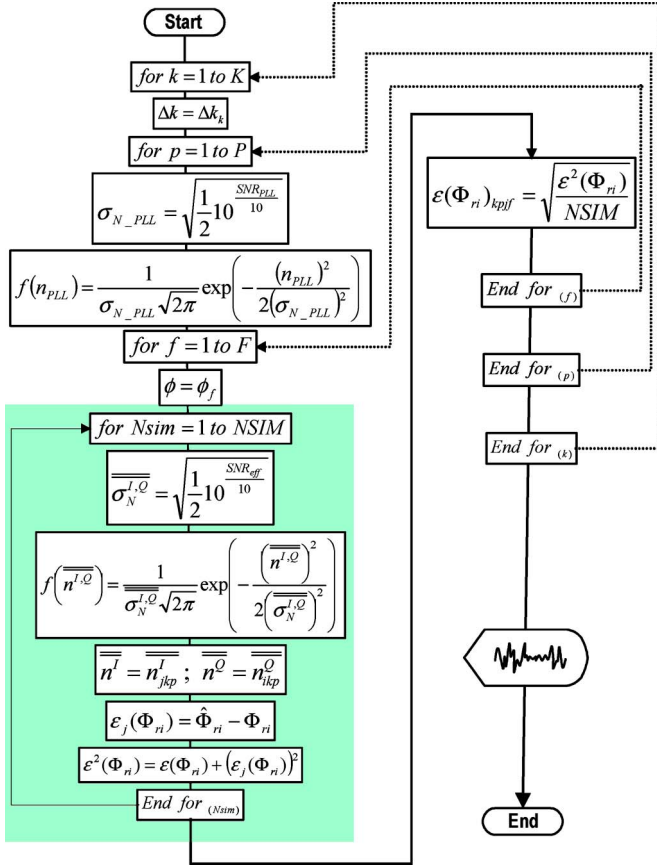


Fig. 7. Flowchart of the procedure for SNR-threshold finding, attending to precision requirements.

as the standard deviation from simulation tests. After a set of NSIM number of simulations, the error is obtained as

$$\begin{aligned}
 \varepsilon(\Phi_{ri}, \text{SNR}_{\text{eff}}; \Delta k, \text{SNR}_{\text{PLL}}) &= \sqrt{\text{E}[(\varepsilon_j(\Phi_{ri}))^2]} \\
 &= \sqrt{\frac{1}{\text{NSIM}} \sum_{j=1}^{\text{NSIM}} (\varepsilon_j(\Phi_{ri}))^2} \\
 &= \sqrt{\frac{1}{\text{NSIM}} \sum_{j=1}^{\text{NSIM}} (\hat{\Phi}_{ri,j} - \Phi_{ri})^2}.
 \end{aligned} \tag{16}$$

As a result, as shown in Fig. 8, a set of precision curves (one-sigma margin) in distance versus phase can be depicted as a function of SNR_{eff} (indicated over the error trace) for different values of SNR_{PLL} and ΔK (squared legend in the figure). Therefore, a threshold for the SNR_{eff} , i.e., $\text{SNR}_{\text{eff_TH}}$, can be fixed to achieve a certain precision, and restrictions for SNR_{PLL} and ΔK are imposed as well, rendering hardware design constraints.

As can be observed in Fig. 8, if a precision of 1 cm in the distance is desired, which corresponds to a phase error in (16) of 0.048° , an SNR_{eff} of 65 dB is needed. A maximum gain deviation of 0.1% and a maximum SNR_{PLL} of 40 dB must

be preserved as well. These last two constraints are perfectly acceptable in the hardware design. Although it is not shown in the figures, the tests have been made for a value of 0.1° for the phase offsets ϕ_4^I and ϕ_4^Q , which is also acceptable in the design. This is valid for a range of differential distance measurements from 0 to 17 m. With these requirements, the accuracy in the position of the MR, after solving the positioning equations, will be below 5 cm, as shown in Section VII.

B. Navigation Aspects. MR Movement Constraints

A comment can be made here about the navigation aspects of the MR. The SNR_{eff} has been obtained with an effective 32-Hz-bandwidth low-pass filter (filters F_4 , I and Q, in Fig. 2). This filter is extremely important for the value of $\text{SNR}_{\text{eff_TH}}$ as the total final SNR depends enormously on its bandwidth. The value of ϕ_{ir} changes linearly with the velocity of the MR, considering a simple small straight line displacement at a constant speed while measurement takes place. Knowing that F_4 is a first-order filter, the tracking error of ϕ_{ir} obtained at the output of the filter with respect to the input is computed as the stationary error reached for a slope input. When the speed of the MR is 1 m/s, for 1 cm of error due to the MR movement, the bandwidth of F_4 must be 32 Hz or higher. Should the MR speed be increased by a factor of K_v , the bandwidth of the filter must be widened by the same proportion, but this would again affect the output SNR. As the noise power spectrum is flat in the output-filter bandwidth, the noise power would be worsened proportionally. Therefore, the output SNR would diminish a value of $10 \log(K_v)$ dB. Hence, there is a tradeoff between the velocity of the MR and the precision in the measurement through the output filter bandwidth.

VI. COVERAGE MAPPING

The process for coverage mapping is an offline process of extreme importance for the correct design of the LPS. It provides the areas where the MR position is achieved with a certain fixed precision. With the explanation developed thus far, the areas of valid coverage for the MR in respect to a certain RP are the regions in its movement plane where the SNR measured at that RP is above a fixed threshold level. For a certain electrical noise level considered at a receiver, the validation of good coverage or not at a point in the MR movement space depends on the signal level at that point. Due to the mathematical expression of the signal obtained at the output of the $i-v$ converter given in (1), having rotational symmetry, when \mathbf{u}_{ri} is (0 0 -1), for a single receiver, the coverage area is therefore circular. The intersection of the coverage areas of two receivers RP_i and RP_j is no longer circular. Fig. 9 illustrates all of this. For every single receiver to find the area that meets a certain SNR threshold level, it is necessary to transform the $\text{SNR}_{\text{eff_TH}}$, already defined in the previous section, back into signal level at the reception stage.

Once a certain effective SNR threshold level is fixed for a certain desired precision, the threshold level for K_3 for all the receivers, from (11), is given in (17), shown at the bottom of the next page.

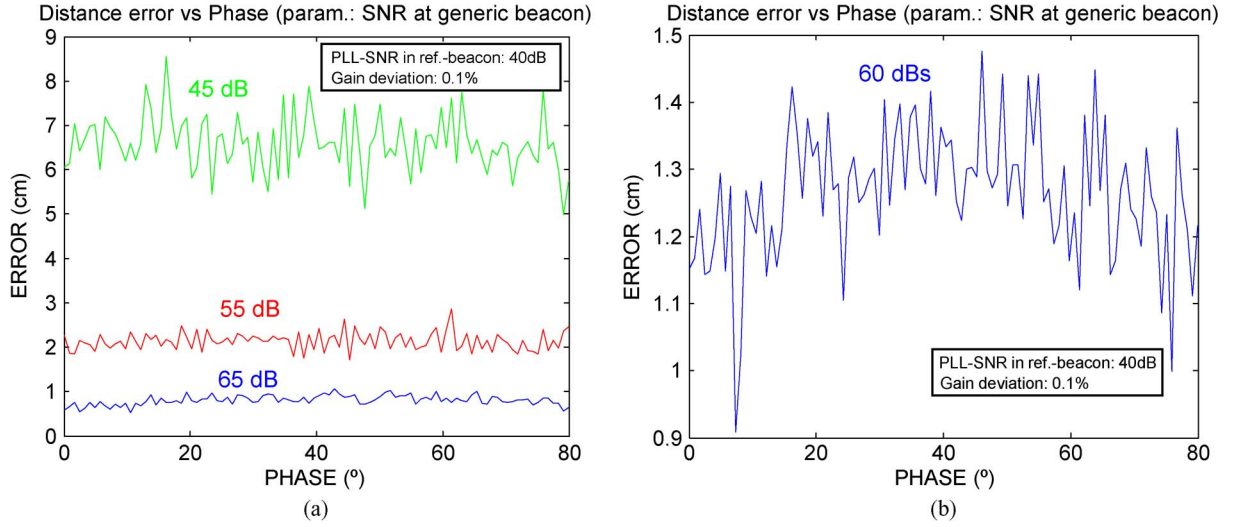


Fig. 8. (a) SNR dependency of phase precision: 45, 55, and 65 dB. (b) Simulation for 60 dB, with a zoomed scale.

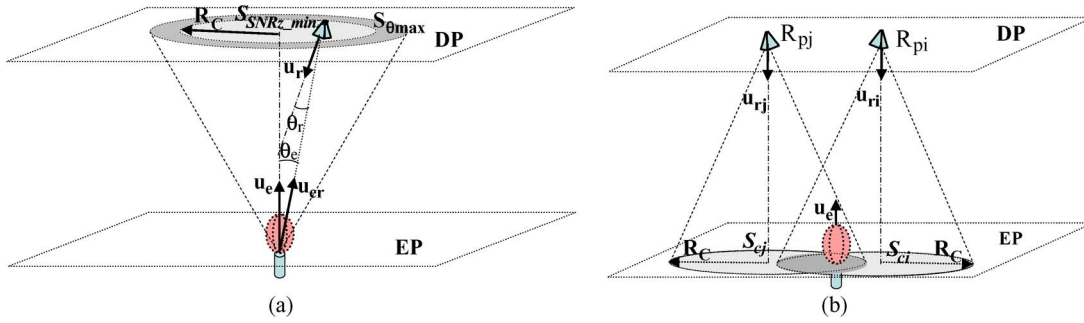


Fig. 9. Coverage definition. (a) Area on the detection plane (DP) reached with SNR below $\text{SNR}_{\text{eff_TH}}$ from the emitting plane (EP) (may be smaller than the area covered geometrically, $S_{\theta_{\text{max}}}$). (b) Areas seen by receivers both RP_j and RB_j under the criterion of (a) and intersection of both.

Take

$$N = \max(N_i^I, N_i^Q)$$

$$K_{04i} = \max(K_{04i}^I, K_{04i}^Q)$$

so that the most conservative values are considered for both I and Q branches. Note that N is eventually computed for any generic receiver (i -indexed), as SNR threshold value restrictions must be met by any receivers in the BLC, as what happens for K_{3_TH} , resulting in a threshold value for any K_{3i} . The constant K_{3i} includes all the multiplying constants throughout previous stages, and the original amplitude of the received current signal I_{p0i} , whose rms value is written in (1). Thus

$$K_{3i} = I_{p0i} K_{Zi} K_{02i} K_{03i} \quad (18)$$

where K_{02i} and K_{03i} are the total multiplying constants resulting from the second and third stages, respectively (amplifier A, filter F_2 , multiplier M_3 , and filter F_3 in Fig. 2) and, K_{Zi} is the constant corresponding to the i - v transimpedance transfer function, obtained as

$$K_{Zi} = Z_i(j\omega)|_{\omega=2\pi f_0} \quad (19)$$

where $Z(j\omega)$ is the expression in (3). Finally, the rms current in (1), generated at the i th photodetector, is restricted by $\text{SNR}_{\text{eff_TH}}$ and must meet the following restriction:

$$I_{0i} \leq \frac{1}{\sqrt{2}} \frac{K_{3_TH}}{K_{Zi} K_{02i} K_{03i}} = I_{0i_TH}. \quad (20)$$

$$K_{3_TH} = K_3(\text{SNR}_{\text{TH}}) = \frac{1}{\pi} \sqrt{8 \cdot (\text{KN}_{3i})^2 (K_{04i})^2 N \cdot 10^{\text{SNR}_{\text{eff_TH}}/10}}$$

$$= \frac{1}{\pi} \sqrt{8 \cdot (\text{KN}_{3i})^2 (K_{04i})^2 2\text{BW}_{\text{Neq}} \sum_{n=0}^{\infty} \frac{\eta_n}{(2n+1)^4} \cdot 10^{\text{SNR}_{\text{eff_TH}}/10}} \quad (17)$$

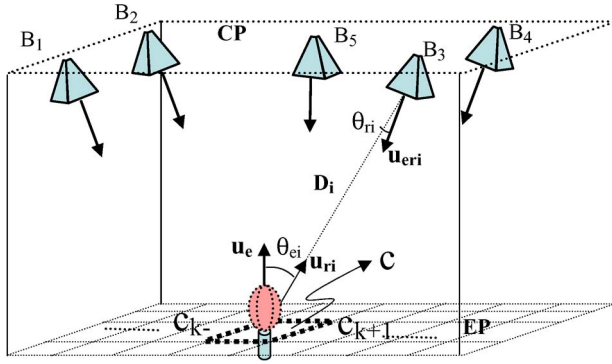


Fig. 10. Elementary subcell (c_k) for valid coverage checking.

The factor $\sqrt{2}$ has been introduced because the rms value of the current is taken. The threshold value K_{3_TH} is computed as in (17), and I_{oi} has the expression shown in (1). The current value I_{OI_TH} is then the threshold level that the amplitude of the photocurrent must have to achieve the minimum SNR necessary to reach the precision desired. Now, as illustrated in Fig. 10, for the LPS-coverage-mapping design, a basic positioning region (BPR) for the MR is defined where the coverage map is traced. It refers to a basic locating cell BLC, already defined, consisting of the minimum number of receivers demanded by the position-calculating system. The BPR is subdivided into small elementary subcells C_k , and for each cell, the current-signal amplitude is checked at every receiver RP_i to verify whether it has a value higher than the threshold level, in which case the cell is considered to be covered by the receiver, tested or not. Thus

$$\begin{aligned} \text{if } I_{0i,k} \geq I_{0_TH}, \quad \text{then } c_{ik} &= 1 \\ \text{if } I_{0i,k} < I_{0_TH}, \quad \text{then } c_{ik} &= 0. \end{aligned} \quad (21)$$

A unique I_{0_TH} has been considered for all receivers. Slight differences in constants K_{Zi} , K_{02i} , and K_{03i} in Fig. 2 will not be appreciable with regard to coverage radii. $I_{0i,k}$ is the amplitude of the current signal generated at the i th receiver in the BLC from the signal that would be emitted from the cell C_k in the BPR, and the value of c_{ik} indicates whether the current value is over the required threshold level or not. The number of receivers covering an elementary subcell is the coverage index (CI) in that subcell so that a minimum CI is defined in the system for a navigation region not to be considered as a dead zone. The CI at C_k , i.e., CI_k , is therefore computed as follows:

$$CI_k = \sum_{i=1}^N c_{ik} \quad (22)$$

with N receivers in a BLC and computing c_{ik} as explained in (21). The coverage map for the BPR is built by representing the CI_k value for every C_k . Some maps for real configurations of the whole system are shown in Section VII.

VII. RESULTS

In this section, a set of results is presented to show the performance of the developed model. First, it is used to study

the coverage areas when any parameter in the model is changed, although only some of them are discussed here, is analyzed; its utility to set the size of cells to cover a real environment is also shown. Afterward, some real tests are also shown to ascertain the validity of the method. For both the simulation cells generated in the first part as well as for the real-tests cell in the latter, the main RP is the one placed in the center of the BLC. The whole configuration is structured in four configuration blocks, as can be seen in Table I, where, for this set of results, they are fixed to the nominal values shown in the table. The most relevant parameters that the model uses are displayed in the table. All the resulting coverage maps shown in this section are formed by areas in the robot BPR in which the differential phase shift is measured with 0.05° precision, which, in turn, corresponds to a 1-cm differential distance precision (one-sigma interval). As can be seen in the table, the detector device is the *NT54-520*, whose features also appear in that table. In Fig. 11, there is, nevertheless, a previous comparison between the coverage areas generated with the *NT54-520*, as well as with the *AEPX65*, whose features are given as follows: responsivity 0.55 A/W ; FOV $\pm 60^\circ$; C_D 6 pF; and A_s 0.5 mm^2 . The BLC for both is a 2-m square cell. Here, there is a tradeoff between the much higher sensitive area of the *NT54* and its higher junction capacitance. The former detector would improve the energy collected at the photodetector, but it implies worse propagation time stability. Moreover, despite the more energy collected, it could also worsen the integrated total noise as its spectral density depends on this capacitance, as shown in (6). However, in this case, the *NT54* is a better device for achieving larger coverage areas.

The effect of a larger sensitive area, i.e., 9 mm^2 , is depicted in Fig. 12(b); the photocurrent amplitude in (1) gets higher proportionally to A_s , and the threshold level for that current is then reached in more locations of the BPC, as the SNR_{eff} is eventually more favorable despite the effects on the noise power that the larger capacitance could cause. This effect can be achieved, either by working with a larger detector or by attaching an optical arrangement producing an equivalent larger effective area.

The first solution is not always possible, in fact, choosing the device is one of the most critical steps in the development of the system; larger devices bring together serious drawbacks such as a higher C_D and, hence, less response time stability. An optical arrangement is a good tradeoff solution, used in this work, but it also has its limitations, such as a possible worsening FOV. The effect of changing some parameters in the optical arrangement is shown in Fig. 12(c), where using a 25-mm-focal-distance lens, i.e., f' , and an out-of-focus 15-mm separation, i.e., s' , between the lens and the photodetector would generate larger coverage areas (nominal values are $f' = 30 \text{ mm}$ and $s' = 20 \text{ mm}$). Working with a less focal-distance lens would enable larger areas again, but it becomes much more difficult and expensive to achieve. As a real application, a real public building has been considered for coverage mapping. A map of the corner of the building is shown in Fig. 13(b), with the measurements in meters.

Connecting the MR positioning issue to navigation aspects, a possible trajectory is drawn from a starting point to a finishing

TABLE I
MODEL PARAMETER CONFIGURATION VALUES. NOMINAL CONFIGURATION

MOBILE-ROBOT POSITIONING-SPACE		I-V CONVERTER OF RECEPTION STAGE	
BLC (length, width, height) [m]	3×3×3	Operational amplifier	
Receivers (BDC) (number, geometry)	5, square(1 in centre)	IC (ref)	OPA655P
MR height (cm)50		Noise-voltage density (V_n [V/ $\sqrt{\text{Hz}}$])	$6 \cdot 10^{-9}$
		Noise-current density (I_n [A/ $\sqrt{\text{Hz}}$])	$1.3 \cdot 10^{-15}$
OPTICAL AND OPTOELECTRONIC DEVICES		Open-loop intrinsic-pole [Hz]	$2.4 \cdot 10^5$
Emitter		Input capacitance (C_{in} [pF])	2.2
Device (ref)	HIRL5012	Feedback impedance	
Max emitting power (I_{e0}) [mW/Sr]	80 (I_{DC} : 100mA)	R_f [Ω]	$7.1 \cdot 10^3$
Lambertian index (n)	1	C_f [pF]	4.7
Detector		Non-inverting-input impedance	
Device (ref)	NT54-520L (PIN)	R_{ni} [Ω]	$8.2 \cdot 10^3$
Junction capacitance (C_D) [pF]	15	C_{ni} [nF]	1
Responsivity (R) [A/W]	0.55 ($\lambda=850\text{nm}$)	SIGNAL-TREATMENT INSTRUMENTATION STAGE	
FOV [$^\circ$]	± 60	Noise-filtering bandwidth (BW_{F4}) [Hz]	32 (active, ord. 1)
Sensitive area (A_s) [mm 2]	5.1	Multiplying constants	
Optical arrangement		Trans-impedance stage: $K_{01} \cdot K_z$ [V/A]	$852 \cdot 10^3$
Lens focal-distance [mm]	25	2 nd stage: K_{02}	0.97
Lens-to-detector distance [mm]	15	3 rd stage: K_{03}	0.98

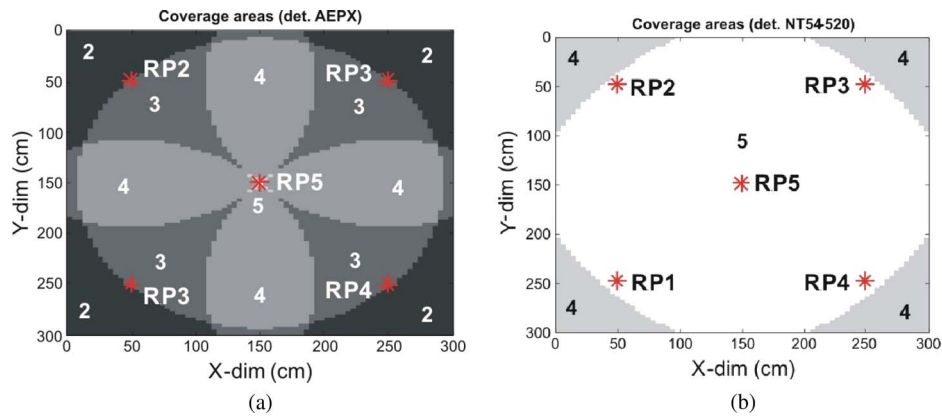


Fig. 11. Comparison between coverage areas with two detectors. A 2-m-side square-shaped BLC (2-m separation between RPs) with a receiver in the center is considered for both. Detectors: (a) AEPX and (b) NT54.

point (circled points S and E in the figure, respectively), passing through the intermediate points 1, 2, and 3 (also circled in the figure). In Fig. 14, four different BDCs are depicted that have been generated to cover the area of the building where the trajectory is, while in Fig. 15, the coverage inside the building is carried out. In the large square-shaped corner, the trajectory goes from point S to 1, the BDC is the 3-m square one, as shown in Fig. 14, which is larger than the others depicted in the same figure and is also applied to cover a larger BPC. There is a

tradeoff between exhaustive coverage and the number of BLCs and, therefore, the number of receivers. In this case, as shown in Fig. 15(a), there are several points along the MR trajectory under the maximum CI, i.e., 5, with the rest of the path under a CI of 4, it is, nevertheless, possible for the MR to be positioned, although with a higher error. In both the link between points 1 and 2 of the trajectory and the corridor between points 3 and E , a rectangular cell with dimensions 1.2×3 m, as shown in Fig. 14(c), is situated. The CI is indicated in the figure showing

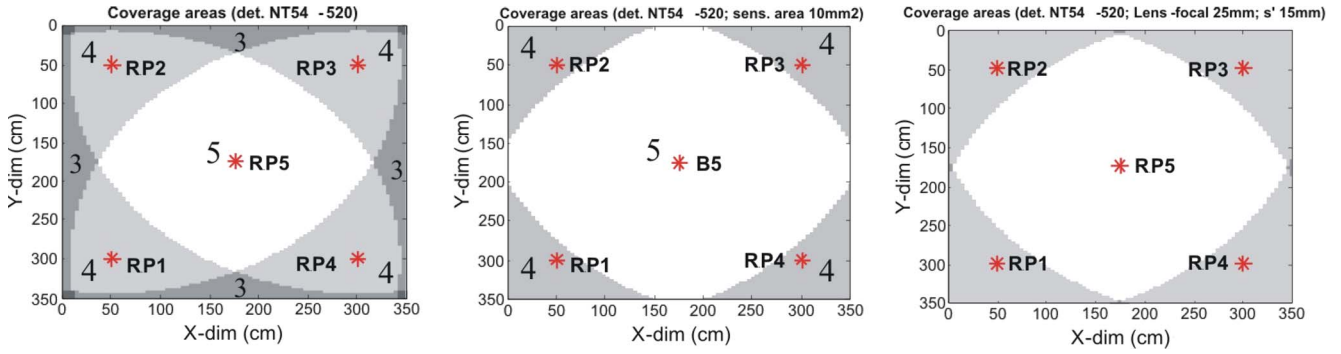


Fig. 12. (a) BPC with 2.5-m side (separation between RPs) for the NT54. (b) Effect of a larger sensitive area, $A_s = 9 \text{ mm}^2$ on the same cell. (c) Effect of a lens focal distance of 25 mm and *out-of-focus* 15-mm separation.

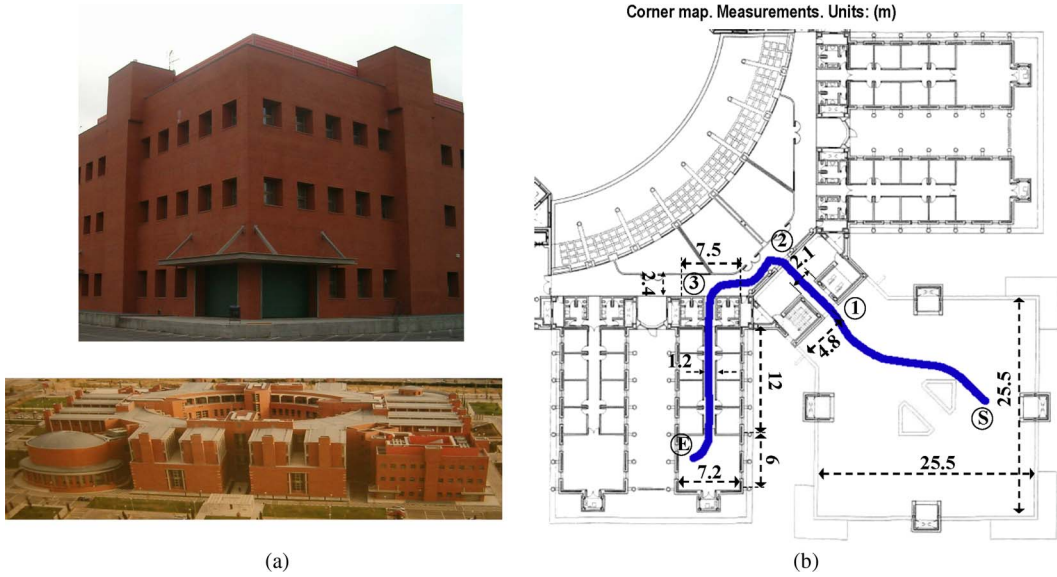


Fig. 13. (a) Public building (Sup-Eng. School) and the corner to be covered. (b) Corner map and MR trajectory from point *S* to *E*, through points 1, 2, and 3.

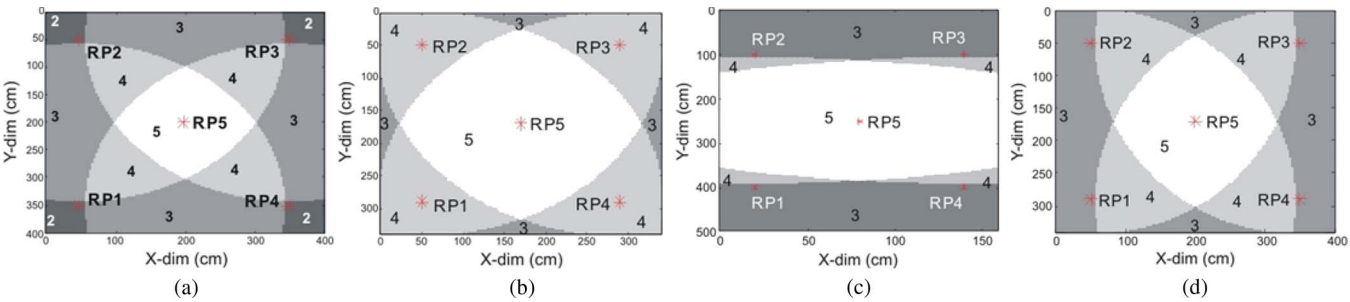


Fig. 14. Cells for covering the selected area. Numbers indicate the coverage index. Cells for (a) large square corner, link between points *E* and 1, (b) link between points 1 and 2 and between 2 and 3 of the trajectory, (c) corridor, link between points 3 and *E* (c), and (d) square-shaped end of the corridor.

certain areas with $CI = 3$; in any case, in a straight corridor, it is possible to have nonsupervised navigation along a longer path. For points 2 and 3 in the trajectory, a 2.4-m square cell has been designed to fit the width of the corridor, as depicted in Fig. 14(b). In this case, the whole segment crosses the maximum-coverage areas. Finally, at the end of the corridor, a square room is covered with the cell shown in Fig. 14(d), which is designed with specific dimensions for this area as well.

A. Real Tests

In Fig. 16(a), the circuit board designed specifically for the receiver is shown. It has been designed to take special care of the noise considerations explained in Section II, as the first stage is the noisiest stage in the system. After the demodulation stage, for every differential measurement, two dc signals like the ones shown in Fig. 16(b) are ready in the PC to obtain

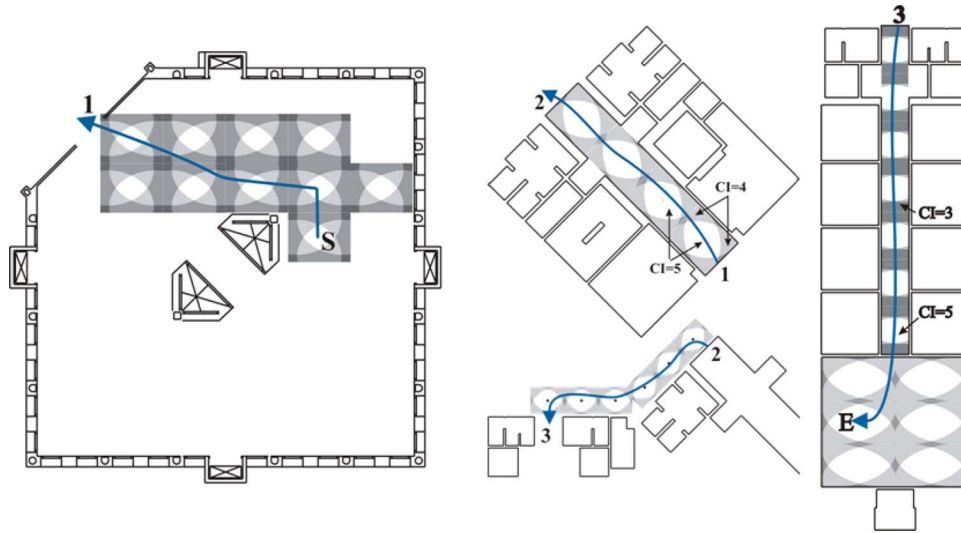


Fig. 15. Covered areas suitable for robot positioning and navigation. Trajectory is divided into segments between the starting point *S* and the finishing point *E*.

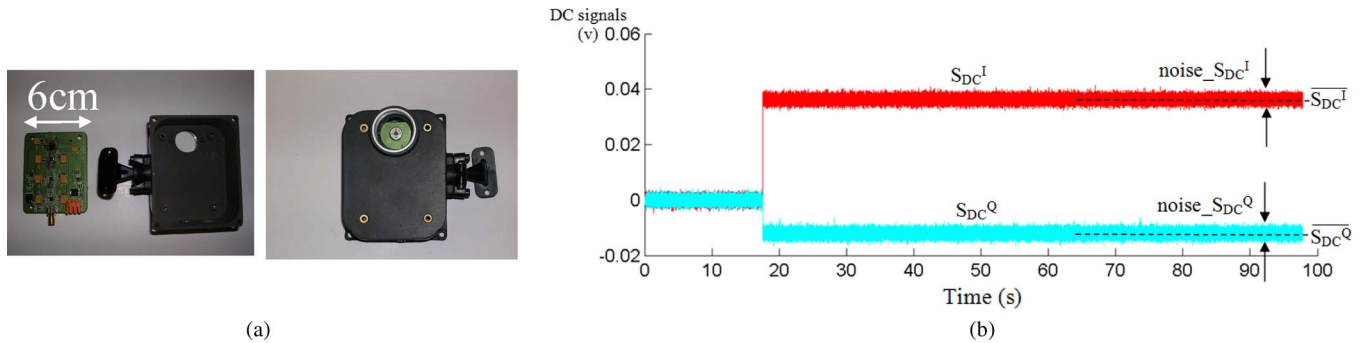


Fig. 16. (a) Sensor printing circuit board (PCB) and specific case for it, prepared to attach an optic element; final dc signals. (b) Average values are close to true values with great accuracy after calibration (first 100 samples). Additive noise is present, increasing with distance and affecting an individual sample as shown.

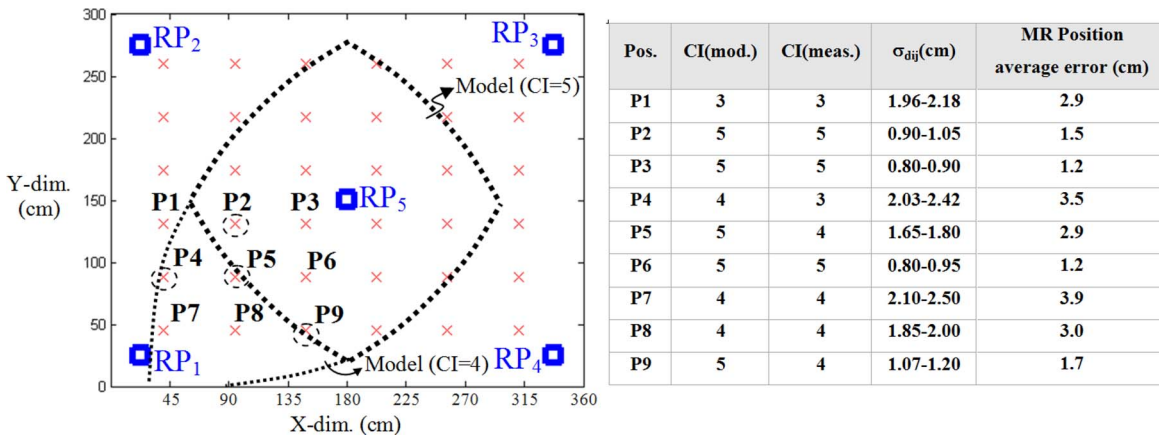


Fig. 17. Grid test for method validation and table of results.

the DPOA and compute the position. In that signal trace, time scale does not fit real-time performance constraints as the image corresponds to real signals but in laboratory experiments for further signal processing (averaging, dispersion calculations, stability analysis, and so forth). Actually, the system performs acquisition in a few milliseconds.

The first validation measurements have been taken on a test grid in a cell with the dimensions of the one labeled as (d) in Fig. 14 because the system itself is being developed in the

squared area at the end of the trajectory considered in Fig. 13, where this cell suits. This grid test is shown in Fig. 17, where only the positions in the bottom-left sector are labeled and discussed, as long as the rest of the sectors of the grid test keep symmetry with respect to the one under consideration. In the table to the side, the standard deviation values of the differential distances calculated from the DPOA measurements for every labeled position can be seen (the intervals shown take into account different measurement sessions). The CIs predicted by

the model and the one assigned from the measurements are depicted as well in that table for comparison. Note that the SNR_{eff} defined in this paper is a threshold value at each tested position for all the RPs, given by the one receiving the lowest signal level from the MR. In the sector under analysis in the figure, this worst signal RP is RP_3 . Thus, the σ -values shown correspond to the measurements between the main RP and RP_3 . The main RP in this test is the central one, i.e., RP_5 . Note that the main RP presents no additive noise problems as its signal is cleaned by a PLL (as long as it has a minimum signal level, enough for the PLL to track properly), transforming its additive amplitude noise into phase noise; nevertheless, this noise is well inside the margin needed for the desired precision, as explained in Section V-A. As can be seen, although the points P_5 and P_9 are placed in the four-index coverage area from the measurements, they are predicted to be in the five-index one. Nevertheless, these points belong to the edge of the area, hence, the predicted cell and the modeled one are still quite close. Point P_4 also mismatches, as it is placed outside the area with index 4, although it was predicted to be inside that area, but again, it is a border point. However, it would be of great interest to improve the accuracy of the definition of the areas under the coverage of four RPs, as four of them could be used to estimate a position, although less accurately than if five RPs were used. A reason for the little mismatch between both cells is that the transmitter is delivering slightly lower power than it theoretically should, due to small PCB artifacts. An enhanced version is currently in progress and promises improved results. With the results thus far, the cell under real test is acceptably close to the theoretical one. On the theoretical side, future work should focus on studying other possible estimators from the observations (i.e., the dc signals measurement) and, on the practical side, should extend measurements to other cells with different shapes.

In our system, the differential ranges measured are used to solve the positioning set of equations in the computer. With this purpose, a nonlinear least squares (NLLS) estimation, plus a Gauss–Newton iteration method for solving the NLLS resulting optimization equation, has been implemented in the PC. The error in the position obtained, which is considered as the distance between the estimated position and the true one, has been also shown in the table in Fig. 17 as an average from all the tests.

The NLLS estimator performs for unbiased random variables. Hence, a high noncorrected bias error, coming, for instance, from an error in the position of the RPs, would affect the interpretation of the results and lead to wrong conclusions. In our case, the position of the location RPs can be known with an acceptable accuracy (a few millimeters), and it does not severely affect the precision in the MR position; this is ascertained by the solution obtained from real measurements.

VIII. CONCLUSION

A global methodology for connecting instrumentation aspects to navigation issues, such as generating a coverage map for an MR in an IS, has been shown. Precision constraints have been related to SNR restrictions by means of a measurement estimator and by translating the effective SNR back to the SNR

at each receiver, also locating RPs in our system. The coverage shown is quite exhaustive, but more separated coverage cells could be used if the MR was able to navigate longer distances unsupervised, using odometry.

The system has been accurately fitted so that for a precision of about 1 cm in distance measurement, an effective SNR of 65 dB is needed at the last stage of the electronic block, filtering signal and noise with an effective low-pass narrow-bandwidth filter, with a 100-Hz 3-dB cutoff frequency; the SNR at the reception stage is much lower. With this SNR threshold detection cells, consisting of five detecting RPs, with side dimensions of around 2 m are achieved. With this cell, the MR position can be known with an accuracy between 1.5 and 5 cm, which is completely acceptable for mobile-robotics applications. A 1-m/s linear velocity for the MR has been considered as a constraint; it can be increased, although it may worsen SNR. It is not easy to improve on these constraints because of the strong tradeoff between all the parameters involved: opening the angle of the emitter to reach wider areas implies less signal level at the detector; choosing a larger detector device to collect more energy also carries worse propagation time (larger and less stable) of the detecting stage; and finally, any optical arrangement also has a severe tradeoff between FOV and power-level collection.

It has been shown how the model is able to help in designing a system with better performance through simulation, taking into account all the elements integrating the system. Any other parameter of the model can be tuned like the ones shown to evaluate its effect on the coverage areas. The feasibility of the LPS designed according to the method developed has also been tested satisfactorily. The model can easily be improved if the system becomes more complex, and the methodology can be applied to other systems of this nature, even if they have different measuring hardware. The first measurements made to ascertain the validity of the model, performed on one of the cells modeled are quite promising and favor improving the method and going further into the measurements so that a model as close to reality as possible can be achieved and used as a good design tool in further development.

REFERENCES

- [1] J. H. Lee and H. Hashimoto, "Intelligent space," in *Proc. IEEE/RSJ Int. Conf. Intell. Robots Syst.*, Oct./Nov. 2000, pp. 1358–1363.
- [2] J. H. Lee, K. Morioka, N. Ando, and H. Hashimoto, "Cooperation of distributed intelligent sensors in intelligent environment," *IEEE/ASME Trans. Mechatronics*, vol. 9, no. 3, pp. 535–543, Sep. 2004.
- [3] P. Corke and D. Rus, "Localization and navigation assisted by networked cooperating sensors and robots," *Int. J. Robot. Res.*, vol. 24, no. 9, pp. 771–786, Sep. 2005.
- [4] P. Corke, R. Peterson, and D. Rus, "Networked robots: Flying robot navigation using a sensor net," in *Proc. Int. Symp. Robot. Res.*, Oct. 2003, pp. 234–243.
- [5] C. Pradalier and S. Sekhavat, "Localization space: A framework for localization and planning, for systems using a sensor/landmarks module," in *Proc. IEEE Int. Conf. Robot. Autom.*, Washington, DC, May 2002, pp. 708–713.
- [6] J. J. Caffery, Jr. and G. L. Stüber, "Overview of radiolocation in CDMA cellular systems," *IEEE Commun. Mag.*, vol. 36, no. 4, pp. 38–45, Apr. 1998.
- [7] E. Aitenbitchler and M. Mühlhäuser, "An IR local positioning system for smart items and devices," in *Proc. 23rd Int. Conf. Distrib. Comput. Syst. Workshops*, May 2003, pp. 334–339.

- [8] Y. Arai and M. Sekiai, "Absolute positioning measurement system for mobile robot based on incident angle detection of infrared light," in *Proc. IEEE/RSJ Int. Conf. Intell. Robots Syst.*, Las Vegas, NV, Oct. 2003, pp. 986–991.
- [9] J. Kahn and J. Barry, "Wireless infrared communications," *Proc. IEEE*, vol. 85, no. 2, pp. 265–298, Feb. 1997.
- [10] S. Poujoly, B. Jourmet, and D. Miller, "Laser range finder based on fully digital phase-shift measurement," in *Proc. 16th IEEE Int. Conf. Instrum. Meas. Technol.*, May 1999, pp. 1773–1776.
- [11] A. Kilpelä, "Pulsed time-of-flight laser range finder techniques for fast, high precision measurement applications," Ph.D. dissertation, Dept. Elect. Inf. Eng., Univ. Oulu, Oulu, Finland, 2004.
- [12] K. Määttä and J. Kostamovaara, "A high-precision time-to-digital converter for pulsed time-of-flight laser radar applications," *IEEE Trans. Instrum. Meas.*, vol. 47, no. 2, pp. 521–536, Apr. 1998.
- [13] P. Palojarvi, K. Määttä, and J. Kostamovaara, "Pulsed time-of-flight laser radar module with millimeter-level accuracy using full custom receiver and TDC ASICs," *IEEE Trans. Instrum. Meas.*, vol. 51, no. 5, pp. 1102–1108, Oct. 2002.
- [14] J. Nissinen and J. Kostamovaara, "Wide dynamic range CMOS receivers for a pulsed time-of-flight laser range finder," in *IEEE Instrum. Meas. Sci. Technol. Conf.*, Como, Italy, May 2004, pp. 1224–1227.
- [15] P. Palojarvi, T. Ruotsalainen, and J. Kostamovaara, "A 250-MHz BiCMOS receiver channel with leading edge timing discriminator for a pulsed time-of-flight laser range finder," *IEEE J. Solid-State Circuits*, vol. 40, no. 6, pp. 1341–1349, Jun. 2005.
- [16] H. Eren and C. C. Fung, "Position estimation of mobile robots based on coded infrared signal transmission," *IEEE Trans. Instrum. Meas.*, vol. 46, no. 6, pp. 1280–1283, Dec. 1997.
- [17] M. Hebert, "Active and passive range sensing for robotics," in *Proc. IEEE Int. Conf. Robot. Autom.*, San Francisco, CA, Apr. 2000, pp. 102–110.
- [18] J. B. Carruthers and J. M. Kahn, "Angle diversity for nondirected wireless infrared communication," *IEEE Trans. Commun.*, vol. 48, no. 6, pp. 960–969, Jun. 2000.
- [19] F. Giuffrida, P. Morasso, G. Vercelli, and R. Zaccaria, "Active localization techniques for mobile robots in the real world," in *Proc. IEEE Conf. IROS*, Nov. 1996, pp. 1312–1318.
- [20] J. S. Esteves, A. Carvalho, and C. Couto, "Generalized geometric triangulation algorithm for mobile robot absolute self-localization," in *Proc. IEEE Int. Symp. Ind. Electron.*, Jun. 2003, pp. 346–351.
- [21] A. Easton and S. Cameron, "A Gaussian error model for triangulation-based pose estimation using noisy landmarks," in *Proc. IEEE Int. Conf. Robot., Autom. Mechatronics*, Dec. 2006, pp. 1–6.
- [22] M. Walworth and A. Mahajan, "3-D position sensing using the differences in the time-of-flight from a wave source to various receivers," *IEEE Trans. Robot. Autom.*, vol. 17, no. 1, pp. 91–94, Feb. 2001.
- [23] H. Suzuki, "Accurate and efficient prediction of coverage map in an office environment using frustum ray tracing and in-situ penetration loss measurement," in *Proc. 57th IEEE Int. Veh. Technol. Conf.*, Apr. 2003, pp. 236–240.
- [24] L. D. L. Perera, W. S. Wijesoma, and M. D. Adams, "The estimation theoretic sensors bias correction problem in map aided localization," *Int. J. Robot. Res.*, vol. 25, no. 7, pp. 645–667, Jul. 2006.
- [25] E. Martín, J. L. Lázaro, I. Bravo, P. Revenga, and P. Ramos, "A local positioning system based on pseudo random sequence emission," in *Proc. IFAC*, Barcelona, Spain, Jul. 2002.
- [26] W. H. Foy, "Position-location solutions by Taylor-series estimation," *IEEE Trans. Aerosp. Electron. Syst.*, vol. AES-12, no. 2, pp. 187–194, Mar. 1976.
- [27] E. M. Gorostiza, J. L. Lázaro, and J. L. Martín, "LPS system based on fixed detectors," in *Proc. SAAEI*, Matanzas, Cuba, Sep. 2001.
- [28] J. H. Lee, T. Akiyama, and H. Hashimoto, "Study on optimal camera arrangement for positioning people in intelligent spaces," in *Proc. IEEE Int. Conf. RSJ*, Oct. 2002, pp. 220–225.
- [29] B. Jourmet, G. Bazin, and F. Bras, "Conception of an adaptive laser range finder based on phase shift measurement," in *Proc. IEEE IECON*, Aug. 1996, vol. 2, pp. 784–789.
- [30] E. Martín-Gorostiza, J. L. L. Galilea, J. M. G. Domínguez, and A. E. Herrera, "A phase-measuring method to obtain distances applied to a robot positioning system," in *Proc. IEEE Int. Conf. ETFA*, Lisbon, Portugal, Sep. 2003, vol. 2, pp. 216–219.
- [31] R. J. Zavrell, Jr., "New low-power single sideband circuits," Philips Semiconductors, Eindhoven, The Netherlands, Application Note AN1981, Oct. 1997.
- [32] J. M. Kahn, W. J. Krause, and J. B. Carruthers, "Experimental characterization of non-directed indoor infrared channels," *IEEE Trans. Commun.*, vol. 43, no. 234, pp. 1613–1623, Feb.–Apr. 1995.
- [33] J. B. Carruthers and J. M. Kahn, "Modeling of nondirected wireless infrared channels," *IEEE Trans. Commun.*, vol. 45, no. 10, pp. 1260–1268, Oct. 1997.
- [34] N. Alsindi, X. Li, and K. Pahlavan, "Analysis of time of arrival estimation using wideband measurements of indoor radio propagations," *IEEE Trans. Instrum. Meas.*, vol. 56, no. 5, pp. 1537–1545, Oct. 2007.
- [35] H. Yang and C. Lu, "Infrared wireless LAN using multiple optical sources," *Proc. Inst. Elect. Eng.—Optoelectron.*, vol. 147, no. 4, pp. 301–307, Aug. 2000.
- [36] G. D. Boreman, "Basic electro-optics for electrical engineers," in *Tutorial Texts in Optical Engineering*, vol. 31. Bellingham, WA: SPIE, 1998.
- [37] P. H. Sidenham, Ed., *Handbook of Measurement Science*. Bognor Regis, U.K.: Wiley-Interscience, May 1986, vol. 1, ch. 8.
- [38] J. G. Proakis and M. Salehi, *Communication Systems Engineering*. Englewood Cliffs, NJ: Prentice-Hall, 2002, pp. 229–231.



Ernesto Martín-Gorostiza received the M.S. degree in physics, with specialty in electronics, from the Complutense University of Madrid, Madrid, Spain, in 1995.

From 1995 to 1997, he was with the Energy, Environment and Technology Research Centre (CIEMAT), Madrid, working in the area of sensors for the electronics department, particularly in electronic systems for thermoluminescence dosimeters. Since 1997, he has been a Lecturer with the Department of Electronics, University of Alcalá, Madrid.

His current research areas are infrared sensorial systems for mobile robotics and mobile robot absolute-positioning systems.



Fco Javier Meca received the B.S. degree in telecommunication engineering from the Polytechnic University of Madrid, Madrid, Spain, in 1994 and the Ph.D. degree in electrical and electronic engineering from the University of Alcalá, Madrid, in 2001.

He is currently an Associate Professor with the Department of Electronics, University of Alcalá. His current work covers the areas of monitoring and control of industrial processes and measurement systems for environmental applications.



José Luis Lázaro Galilea received the B.S. degree in electronic engineering and the M.S. degree in telecommunication engineering from the Polytechnic University of Madrid, Madrid, Spain, in 1985 and 1992, respectively, and the Ph.D. degree in telecommunication from the University of Alcalá, Madrid, in 1998.

Since 1986, he has been a Lecturer with the Department of Electronics, University of Alcalá, where he is currently a Professor. His research interests include robotics sensorial systems by laser, optical

fibers, infrared and artificial vision, motion planning, monocular metrology, and electronics systems with advanced microprocessors.



Eduardo Martos-Naya received the M.S. and Ph.D. degrees in telecommunication engineering from the University of Málaga, Málaga, Spain, in 1996 and 2005, respectively.

In 1997, he joined the Department of Communication Engineering, University of Málaga, where he is currently an Associate Professor. His research interests include performance analysis of communication systems and digital signal processing.



Fernando B. Naranjo was born in Madrid, Spain, on November 4, 1974. He received the M.S. degree in physics from the Complutense University of Madrid, Madrid, in 1997 the Ph.D. degree in physics from the Polytechnic University of Madrid in 2003.

Since 2004, he has been an Assistant Professor with the University of Alcalá, Madrid, where he is a member of the Photonics Engineering Group (GRIFO), where he is currently working on future semiconductor-based photonic devices for all optical communication networks, from basics to device

application level.

Dr. Naranjo received an award from the Polytechnic University of Madrid for his Ph.D. thesis in 2005.



Óscar Esteban was born in Madrid, Spain, in 1970. He received the M.S. and Ph.D. degrees in physics from the Complutense University of Madrid, Madrid, in 1997 and 2001, respectively.

Since 2001, he has been an Assistant Professor with the University of Alcalá, Madrid, where he is also a member of the Photonics Engineering Group (GRIFO). His main research interests include optical-fiber sensors, optical testing of materials, thin solid films, and optoelectronics applications.